

www.acsmaterialsletters.org

Mapping the Complete Reaction Energy Landscape of a Metal—Organic Framework Phase Transformation

Sylvia L. Hanna, Michael Barsoum, Tekalign Terfa Debela, Christos D. Malliakas, Madeleine A. Gaidimas, Julia G. Knapp, Kent O. Kirlikovali, Christopher H. Hendon, Vinayak P. Dravid, and Omar K. Farha*



Cite This: ACS Materials Lett. 2023, 5, 2518-2527



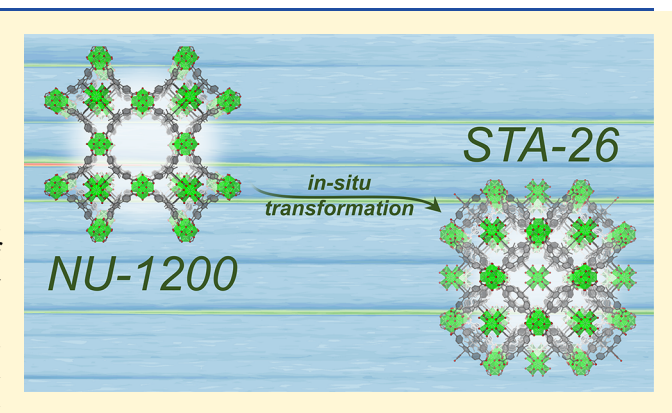
ACCESS I

III Metrics & More

Article Recommendations

s Supporting Information

ABSTRACT: Crystalline materials undergo valuable phase transformations, and the energetic processes that underlie these transformations can be fully characterized through a combination of thermodynamic and kinetic studies. Here, we report the first complete reaction energy landscape of metalorganic framework (MOF) interpenetration, specifically in the phase transformation of NU-1200 to its doubly interpenetrated counterpart, STA-26. We characterized the thermodynamics of this phase transformation by pairing experiments with density functional theory (DFT) calculations. This analysis revealed that factors such as the increase in crystal density likely drive Zr- and Hf-NU-1200 to STA-26 interpenetration, while other chemical interactions such as steric repulsions prevent Th-NU-1200 from



interpenetrating. Using time-resolved in situ X-ray diffraction, we monitored phase transformation reaction profiles and extracted quantitative kinetic information using the Avrami-Erofe'ev model. As a result, we obtained activation energies for the Zr- and Hf-NU-1200 transformations to Zr- and Hf-STA-26, respectively, revealing slower phase change kinetics for MOFs with stronger bonds. Finally, we paired the kinetic data with experimental observations to classify the mechanistic model of this phase transformation as partial dissolution. We anticipate that this thermodynamic, kinetic, and mechanistic understanding will broadly inform further studies on the energetics of crystallization.

In all fields of chemistry, the energetic principles of thermodynamics and kinetics characterize transformations from one state, phase, or isomer to another. 1,2 Thermodynamics concerns itself with the relative stabilities of the starting and ending states on a potential energy surface. The free energy difference between these states (ΔG) describes whether the phase transformation is endergonic (uphill) or exergonic (downhill). While equilibrium and its surrounding effects lie at the heart of thermodynamics, kinetics addresses the pathway to reach equilibrium. How much energy does the system require to break bonds in the first phase and form bonds in the second? The activation energy (E_a) , which identifies the barrier to reaching the transition state and eventual equilibrium (Scheme 1), answers these kinetic questions.³ Although thermodynamics and kinetics stand distinctly apart, their implications intimately couple. 1,4,5 Pairing the two complementary concepts unearths the complete picture of the phase transformation occurring and can provide deeper mechanistic

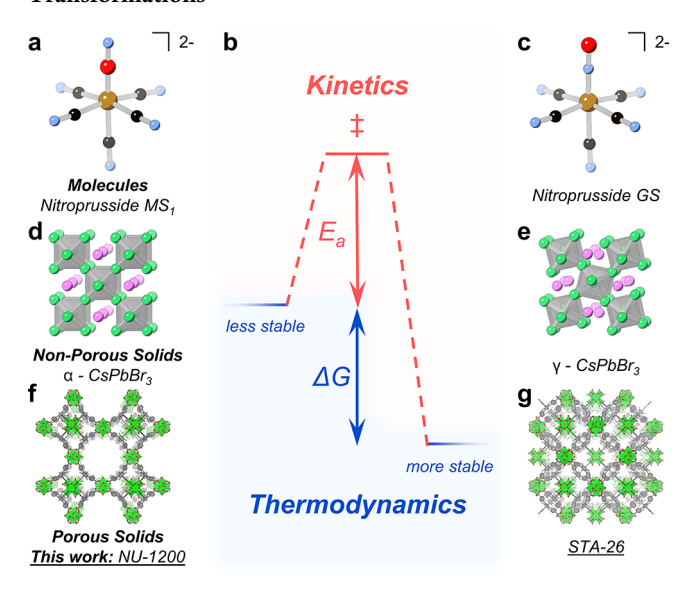
revelations about how chemical interactions within the system lead to the observed product.

Energetically characterizing phase transformations thus carries profound implications for rational design of chemical structures and control of physicochemical properties in systems ranging from molecules ^{6,7} to materials. ^{8,9} For example, ligand rearrangements in sodium nitroprusside provide insight into its medicinal usage for hypertension; ^{10,11} phase transformations in crystalline solids like perovskites and layered metal oxides affect their performance in optical applications, thermoelectricity, and superconductivity (Scheme 1). ^{5,12–14}

Received: June 4, 2023 Accepted: August 2, 2023



Scheme 1. Kinetics and Thermodynamics of Phase Transformations a



 a (a) Metastable MS₁ isomer of sodium nitroprusside with an oxygenbound ambidentate N–O ligand. (b) Exergonic phase transformation from a less stable to a more stable state. (c) Ground state GS isomer of sodium nitroprusside with a nitrogen-bound ambidentate N–O ligand. (d) Less stable cubic α phase of perovskite CsPbBr₃. (e) More stable orthorhombic γ phase of perovskite CsPbBr₃. (f) Less stable MOF NU-1200 and (g) its more stable interpenetrated phase, STA-26

While less explored than their molecular or classical solid-state counterparts, porous crystalline solids such as metalorganic frameworks (MOFs)^{15,16} also benefit from thermodynamic and kinetic characterization of their phase transformations.^{17–20} Comprised of self-assembled metal nodes and organic linkers, MOFs reticulate into three-dimensional porous networks (Scheme 1f, g). These frameworks, while crystalline, often behave dynamically,^{21–23} resulting in phase changes and associated variations in performance. For example, the structural response of MOFs to mechanical stress affects their postsynthetic processing for commercialization,^{24,25} flexibility upon adsorption of carbon dioxide and methane influences gas adsorption and storage,^{26–28} and MOF transformations into denser interpenetrated phases impact catalytic activity and gas storage and separations.^{29–31}

MOF phase transformations are often thermodynamically characterized: ^{32–34} researchers study the relative stabilities of starting and ending phases, develop synthetic methods to traverse the potential energy surface between the two, and quantify their differing performances. However, many questions remain regarding the kinetic processes^{35–41} behind these transformations.

In this study, we pair thermodynamics and kinetics to generate a complete energy map of a MOF interpenetration phase change for the first time. We selected the transformation of NU-1200 to its doubly interpenetrated counterpart, STA-26, as our model system for several reasons. 42,43 First, NU-1200 is known to be chemically stable. 44 Second, NU-1200 can be synthesized as various isostructural analogues (Zr-, Hf-, Th-, etc.) where the metal ions possess different atomic radii, *d* vs *f* electrons, and M-O bond energies. 45 Comparing the differences in interpenetration across these isostructural MOFs allows us to assess how metal differences affect inter-

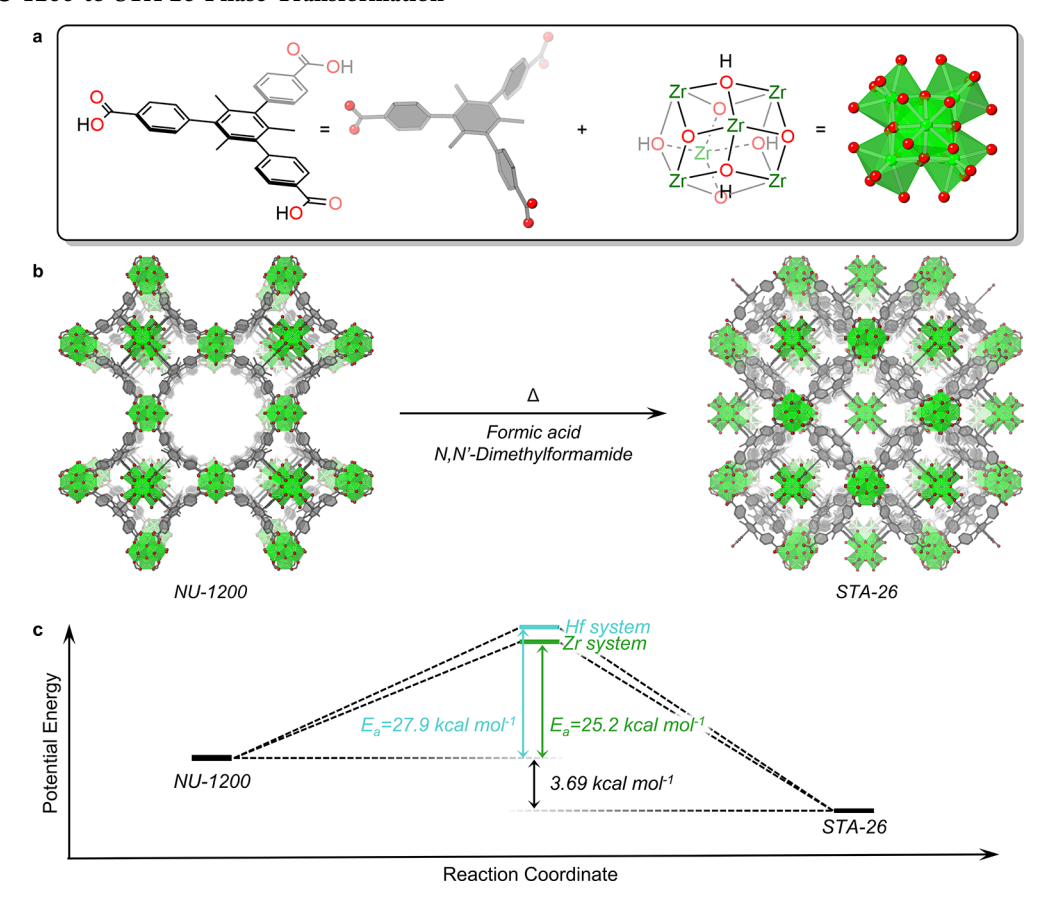
penetration while controlling for the topological and structural similarities between MOFs. Third, the synthetic conditions required to transform NU-1200 to STA-26 are tunable, allowing us to test how specific variables such as temperature affect interpenetration kinetics.⁴⁶

Using in situ time-resolved X-ray diffraction and the Avrami-Erofe'ev model, we monitor phase transformation reaction profiles to extract quantitative kinetic information on interpenetration. Additionally, we confirm that this method of kinetic analysis is sensitive enough to experimentally reveal energetic differences between MOFs with similar metaloxygen bond energies ($\Delta Hf_{Zr-O} = 182 \text{ kcal mol}^{-1}$, and $\Delta H f_{Hf-O} = 189 \text{ kcal mol}^{-1}$). Coupling collected kinetic information with density functional theory (DFT) thermodynamics calculations, we generate a complete map of the NU-1200 to STA-26 transformation on the reaction energy landscape. Finally, we link thermodynamic and kinetic parameters with experimental observations to propose a mechanistic model for this transformation using Avrami exponent values (these range from 0.85 to 1.6 with error values of 0.02-0.1). This report fundamentally investigates the energetics of MOF phase transformations and provides a deeper understanding of interpenetration, influential in applications including gas adsorption, gas separation, and catalysis.³¹ More generally, this study contributes to the rational design of synthetically plausible nanostructures with desirable and controlled chemical properties.

Thermodynamics of NU-1200 to STA-26 Phase Transformation. NU-1200 was first reported in 2016 as a MOF structure consisting of 8-connected $Zr_6(\mu_3-OH)_4(\mu_3-O)_4$ $(OH)_4(OH_2)_4$ nodes and 3-connected 4,4',4"-(2,4,6-trimethylbenzene-1,3,5-triyl)tribenzoic acid (TMTB) linkers (Schemes 2a and S1, Figures S1-S2). 43,44 Zr-NU-1200 can also crystallize in the analogous Hf- and Th-based structures. 45 In 2018, reports of its doubly interpenetrated counterpart, STA-26, surfaced, ⁴² and in 2021, we demonstrated that the Zr-NU-1200 phase can post-synthetically transform to the Zr-STA-26 phase upon the introduction of heat, formic acid, and N,N'-dimethylformamide (DMF) (Scheme 2b).46 Since new linker and node sources are not introduced to the system during the phase transformation, structural components of NU-1200 must contribute to the formation of STA-26 through breaking and forming of chemical bonds. Interpenetration converts the mesoporous Zr-NU-1200 structure with 14 Å sodalite cages and 20 Å channels to the microporous Zr-STA-26 framework comprised of two identical lattices. In STA-26, sodalite cages of the second lattice reside in the channels of the first lattice, introducing $Im\overline{3}m$ centering to the original $Pm\overline{3}m$ Zr-NU-1200 crystal symmetry. Apart from these structural distinctions, the topology persists across both phases, and the cubic unit cell parameters remain very similar (a = b = c =28.33 Å in Zr-NU-1200, and a = b = c = 28.16 Å in Zr-STA-26).

We characterized the thermodynamics of this phase transformation by determining whether the NU-1200 analogs interpenetrate, calculating their relative phase stabilities, comparing the energetic favorability of their interpenetration, and understanding the driving force behind their penchant or failure to interpenetrate. As described previously, pristine Zr-NU-1200 (Figures S5 and S17) converts to Zr-STA-26 (Figure S20a) when exposed to interpenetration conditions, and nitrogen physisorption experiments demonstrate how its two large pores disappear over time and microporous STA-26

Scheme 2. NU-1200 to STA-26 Phase Transformation^a



"(a) Structures of 4,4',4"-(2,4,6-trimethylbenzene-1,3,5-triyl)tribenzoic acid (TMTB) linker, $Zr_6(\mu_3-OH)_4(\mu_3-O)_4(OH)_4(OH_2)_4$ node, and their equivalent visual representations in (b). (b) Transformation of NU-1200 to STA-26. (c) Reaction coordinate diagram of the NU-1200 to STA-26 phase transformation. Diagram not drawn to scale.

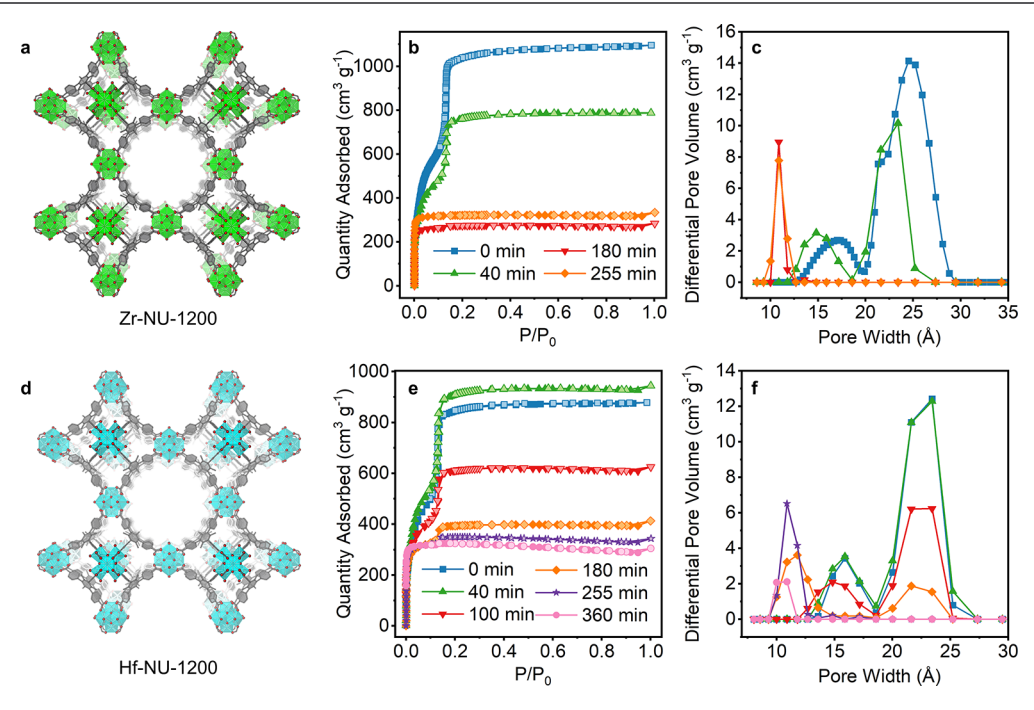


Figure 1. Interpenetration of Zr- and Hf-NU-1200. (a) Zr-NU-1200 and (d) Hf-NU-1200 MOF structures. (b) Nitrogen isotherms and (c) pore size distributions monitoring the interpenetration of Zr-NU-1200 to Zr-STA-26. (e) Nitrogen isotherms and (f) pore size distributions monitoring the interpenetration of Hf-NU-1200 to Hf-STA-26.

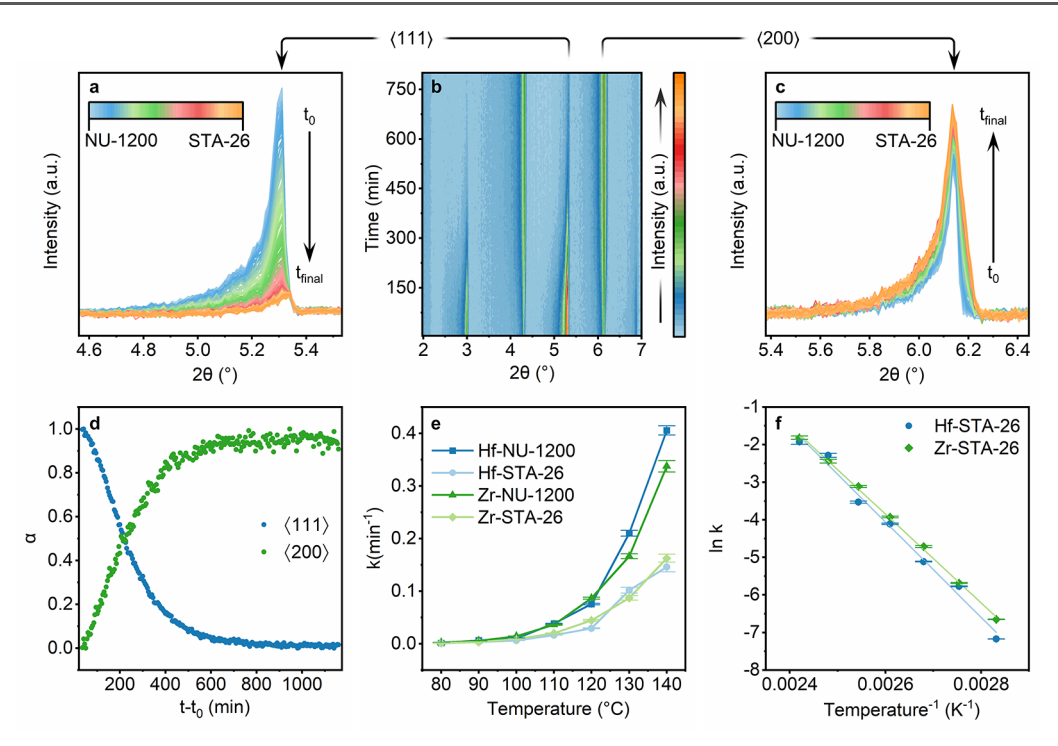


Figure 2. Kinetic analysis of time-resolved diffraction data. (a) Stacked PXRDs enlarged to show the intensity change in the \(\)11\) and (c) \(\)200\) Bragg features in the transformation of Zr-NU-1200 to Zr-STA-26 at 90 °C over time. (b) 3-dimensional contour plot of the first four Bragg features in the transformation of Zr-NU-1200 to Zr-STA-26 at 90 °C. (d) Crystallization curve of Zr-NU-1200 converting to Zr-STA-26 at 90 °C. (e) Extracted Avrami-Erofe'ev rate constants as a function of temperature. (f) Arrhenius plots for Zr- and Hf-STA-26 formations.

appears (Figure 1a-c, Table S3). We attribute the slight increase in uptake, surface area, and pore volume at 255 min to an increase in Zr-STA-26 crystallinity upon its full formation (Supporting Information section 5.3.1). Next, using density functional theory (DFT), we calculated the total energies of the two phases, which showed Zr-STA-26 to be 3.69 kcal mol⁻¹ more stable than Zr-NU-1200 (Figures 1c, S112–S113, Supporting Files). This data suggests that the Zr-NU-1200 to Zr-STA-26 phase change may be driven by the system's ability to access a more stable thermodynamic minimum.

We find that pristine Hf-NU-1200 (Figures S5 and S17) also experiences conversion to Hf-STA-26 under analogous interpenetration conditions (Figure S20b). Nitrogen isotherms reveal a general trend of decreasing uptake, BET surface area, pore volume, and pore width over time (Figure 1d-f, Table S3). Similar to Zr-STA-26, this trend reverses from 180 to 360 min due to an increase in Hf-STA-26 crystallinity upon its full formation (Figure S22, Supporting Information section 5.3.2). Additionally, we attribute the slight increase in uptake, BET surface area, and pore volume after 40 min to defects introduced to the NU-1200 structure by the interpenetration conditions (Figure S21, Supporting Information section 5.3.2). Like its Zr-based analogue, DFT calculations also show Hf-STA-26 as 3.69 kcal mol⁻¹ more stable than Hf-NU-1200 with a similar density of states (Figures 1c, S112–S113, Supporting Files), once again suggesting that the phase change may be driven by the system's ability to access a more stable thermodynamic minimum.

Unlike its Zr- and Hf- counterparts, Th-NU-1200 (Figure S5a) did not interpenetrate under our attempted conditions, as shown by PXRD and sorption experiments (Figures S15, S17–18, Table S3, Supporting Information section 5.1.4). SEM

images of Th-NU-1200 before and after interpenetration attempts revealed that the particles became etched and their edges rounded, suggesting decomposition (Figure S19). Interestingly, DFT calculations still showed Th-STA-26 as 3.69 kcal mol⁻¹ more stable than Th-NU-1200 with similar density of states to its Zr- and Hf- analogs (Figures S112—S113, Supporting Files).

Thus, the Zr-, Hf-, and Th- systems possess nearly identical total energies and similar density of states, work functions, and band gaps (Figure S112), yet they behave differently. Since all three systems chemically differ only by the node identity, these data suggest that the energetic similarities are motivated by common denominators between all MOF analogs, while their behavioral differences may be driven by node identity. Specifically, similar energetic data suggest that the majority of electronic properties are driven by parallels such as ligand chemistry and topology. Additionally, we hypothesize that the driving force for interpenetration in all cases arises from the doubling of the MOF density as NU-1200 transforms to STA-26. Indeed, crystal density has been shown to influence the thermodynamics of crystalline systems dramatically.^{4,48}

Conversely, since the observed lack of interpenetration in Th-NU-1200 is likely driven by the MOF nodes, we hypothesized that the Th_6 cluster nodes may possess additional moieties that hinder interpenetration. We first tested if Th_6 nodes were coordinated to additional formate groups (from modulator decomposition), which could sterically prevent interpenetration. MOF digestion and subsequent NMR experiments proved that fewer formate groups were bound to the Th_6 node than to the Zr_6 or Hf_6 nodes, voiding this hypothesis (Figures S6–S12, Table S2). Next, we examined the Th_6 cluster which can be composed of six nine-coordinated

Th(IV) ions. Unlike the Zr_6 or Hf_6 node clusters, each Th(IV) ion in the Th_6 node cluster coordinates to an additional water molecule, such that the node formula becomes $Th_6(\mu_3-OH)_4(\mu_3-O)_4(OH)_4(OH_2)_{10}$. With this in mind, we hypothesized that the extra H_2O molecules on the Th_6 node may engage in additional hydrogen bonding interactions with water molecules within the MOF pores in which the Zr and Hf analogues do not engage in. This extra network of hydrogenbonded water would increase the effective node size and sterically hinder a second network from interpenetrating. Thermogravimetric analysis/gas chromatography—mass spectrometry (TGA/GC-MS) supported this hypothesis, revealing a continuous and significant release of H_2O (hydrogen-bonded H_2O) from activated Th-NU-1200 until decomposition where a large H_2O release occurred (coordinated H_2O) (Figure S24).

Thus, these data demonstrate that while factors such as the increase in crystal density likely drive NU-1200 to STA-26 interpenetration, these factors can be countered by other chemical interactions like steric repulsions. Taken together, these data define the thermodynamic aspects of the NU-1200/STA-26 system at equilibrium.

Kinetics of NU-1200 to STA-26 Phase Transformation. With the aim of mapping the complete NU-1200 to STA-26 reaction energy landscape, we next investigated the kinetics of its nonequilibrium transformation. How much energy is required to surmount the activation barrier to reach the high-energy transition state? Does the activation energy required to break and form bonds differ between the Zr and Hf systems, which possess similar metal—oxygen bond energies? To answer these questions, we implemented *in situ* time-resolved X-ray diffraction to monitor reaction profiles as a function of temperature. By collecting quantitative kinetic information from single Bragg features with changing intensities, rate constants and activation energies of the phase transformation can be extracted. 38,50,51

Due to the inversion symmetry introduced by centering of the new lattice in STA-26, diffraction peak locations remain constant throughout the phase transformation, while peak intensities change (Figure S20). Intensity changes can be most clearly observed in the first four primary reflections where the (100) and (111) Bragg features (corresponding to the peaks at $3.00^{\circ}2\theta$ and $5.31^{\circ}2\theta$, respectively, in the Zr system and peaks at 3.12 and 5.43°2 θ , respectively, in the Hf system) decay in intensity, while the (110) and (200) Bragg features (corresponding to the peaks at 4.32 and 6.14°2 θ , respectively, in the Zr system and peaks at 4.44 and $6.27^{\circ}2\theta$, respectively, in the Hf system) grow in intensity. Thus, the disappearance of the NU-1200 phase can be monitored by the decay of the (100) and (111) reflection intensities, and the emergence of the STA-26 phase can be monitored by the increase of the (110) and (200) reflection intensities. While the two Bragg features corresponding to a single phase should, in principle, provide the same kinetic information, we monitored both reflections per phase to ensure internal consistency.

We exposed 2 μ m MOF particles to a DMF:FA ratio of 2.5 (Figures S3–S4, Table S1) and tracked the changing reaction profiles of both phases for the Zr and Hf systems at temperatures ranging from 80 to 140 °C (Figure S25). Baseline-corrected representative data for the conversion of Zr-NU-1200 to Zr-STA-26 at 90 °C can be found in Figure 2b, and its most intense Bragg reflections at $\langle 111 \rangle$ and $\langle 200 \rangle$ showing NU-1200 decay (Figure 2a) and STA-26 growth

(Figure 2c), respectively, are highlighted (Figures S26-S104, Table S5).

To quantify the changes in reaction profiles, we calculated the integrated intensities of the primary Bragg features as a function of time (Figure S104). Next, we plotted the normalized peak intensities (α) against the reduced time (t- t_0), defined as the reaction time (t) minus the induction time (t_0), to form crystallization curves (Figures 2d, S26–103). The crystallization curves were then parametrized using the Avrami-Erofe'ev equation, t_0 - t_0

$$\alpha = 1 - \exp\{-(k(t - t_0))^n\}$$
 (1)

By modeling the extent of crystallization (α) as a function of the reduced time $(t-t_0)$, the rate constant (k) and mechanistic crystallization information (n) can be extracted from the sigmoidal curves. ^{38,50} Using a least-squares fit to the Avrami-Erofe'ev model, we extracted rate constants for the NU-1200 disappearance and STA-26 growth in both the Zr and Hf systems (Figures S26–S103, Table S6). Additionally, we verified the Avrami-Erofe'ev sigmoidal fits using its linear equivalent, the Sharp-Hancock equation (eq 2), where n is derived from the slope of the fit line, and n ln(k) is derived from the y-intercept (Figures S26–S103, Table S6). ^{38,50}

$$\ln[-\ln(1-\alpha)] = n \ln(t-t_0) + n \ln(k)$$
 (2)

Both sigmoidal and linear fittings produced comparable results (Table S6), but we employed the Avrami-Erofe'ev fitting values for further analysis due to their lower error. Since kinetic information for NU-1200 decay extracted from the $\langle 100 \rangle$ and $\langle 111 \rangle$ Bragg feature crystallization curves also proved similar, further studies were carried out using the $\langle 111 \rangle$ Bragg feature crystallization curve because of the higher signal-to-noise ratio and cleaner data. Likewise, the $\langle 200 \rangle$ reflection was selected over the $\langle 110 \rangle$ for STA-26 growth.

The extracted kinetic information provides correlations between the NU-1200 disappearance and STA-26 emergence for both Zr and Hf systems. As temperature levels elevate, the reaction kinetic energy rises, and the rates of transformation of both phases subsequently increase (Figures 2e and S105). Although their transformations proceed on concurrent time scales (Figure 2d), STA-26 growth rates consistently lag behind NU-1200 decay rates by an average factor of one-half (Figure 2e, Table S6). This implies that STA-26 growth depends on NU-1200 decay. Indeed, since interpenetration occurs in the absence of new linker and node sources (Scheme 2b), structural components from the first phase must contribute to the second. Related further discussion can be found in the following section.

With quantitative kinetic information in hand, we calculated the activation energies using the Arrhenius equation (Figure 2f). Consistent with their metal—oxygen bond energies $(\Delta Hf_{Zr-O} = 182 \text{ kcal mol}^{-1}, \Delta Hf_{Hf-O} = 189 \text{ kcal mol}^{-1})$, Hf- and Zr-STA-26 formations call for 27.9 and 25.2 kcal mol⁻¹, respectively (Scheme 2c, Table S7). The stronger Hf–O bonds require larger amounts of energy to break and reform than their slightly weaker Zr–O counterparts, resulting in slower kinetics of transformation. Although the Hf and Zr MOFs possess similar metal—oxygen bond energies, this

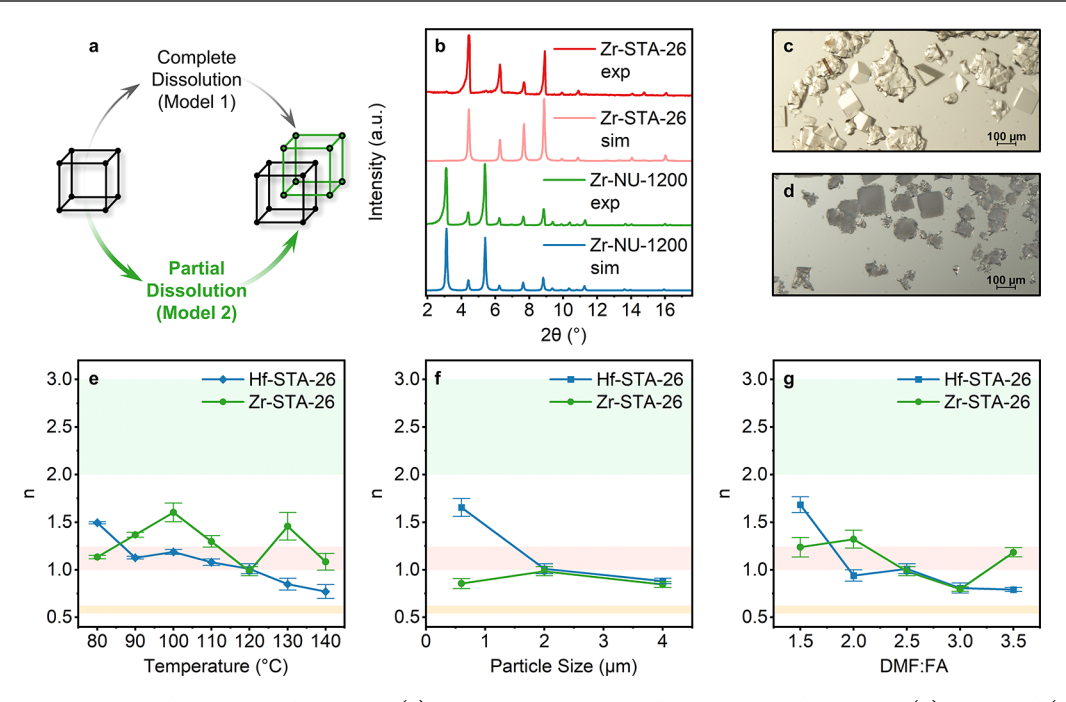


Figure 3. Mechanistic model of phase transformation. (a) Two possible models for phase transformation. (b) PXRD of (c) Zr-NU-1200 crystals converting to (d) Zr-STA-26 crystals. (e) Avrami exponent values at different temperatures, (f) particle sizes, and (g) formic acid concentrations. For (e)-(g), orange panels (bottom) indicate the zero-order region, salmon panels (middle) denote the first-order region, and green panels (top) mark higher-order regions.

kinetic analysis is sensitive enough to experimentally reveal energetic differences between the two systems. Thus, by pairing thermodynamic and kinetic data, we map the full reaction energy landscape of interpenetration in a MOF system for the first time (Scheme 2c).

Mechanistic Model of NU-1200 to STA-26 Phase Transformation. Determining the reaction energy profile can also produce a mechanistic understanding of how chemical interactions within the NU-1200/STA-26 system lead to the observed interpenetrated product. We first characterized the conditions that affect phase transformation and then generated a mechanistic model for conversion.

We hypothesized that conversion of the initial NU-1200 particles likely occurs first from the peripheries and then extends to the core. If this is true, the particle size should influence the rate of transformation, with larger particles transforming slower than smaller particles. We tested the effect of particle size on the conversion rate by comparing the phase transformations of 600 nm, 2 μ m, and 4 μ m Zr- and Hf-NU-1200 particles using time-resolved *in situ* PXRD (Figures S3–S11, S13–S14, S16, Tables S1–S3). Extracted Avrami-Erofe'ev rate constants (units of min⁻¹) show a decrease in the conversion rate at larger particle sizes and support the concept of phase transformation from particle exterior to core (Figures S106 and 108, Tables S5–S6).

In order for the transformation to occur, heat and formic acid must be present. Kinetic differences at increasing temperatures reveal that heat is a source of activation for conversion. If formic acid is also a source of conversion activation, then it thus follows that higher concentrations of formic acid should increase the conversion rate. Time-resolved *in situ* PXRD experiments and extracted Avrami-Erofe'ev rate constants demonstrated that this hypothesized trend held true (Figures S107–108, Tables S5–S6).

To gather deeper insight into the mechanistic model of phase transformation, we investigated the sequential method of conversion. Because interpenetration transpires in the absence of new linker and node sources, it follows that linker and node components from the first NU-1200 phase comprise the structure of the second STA-26 phase. Indeed, as discussed above, correlating conversion rates implies that STA-26 growth depends on NU-1200 decay (Figure 2e). Thus, the phase transformation likely occurs following one of two simplified models: 1) Complete dissolution of NU-1200 into its linker and node building blocks followed by nucleation and growth of new STA-26 particles. 2) Portions of the NU-1200 particles dissolve and produce free linker and node monomers. These monomers then assemble into a second interpenetrated lattice, transforming the NU-1200 particles to STA-26, and nucleation of new particles does not occur (Figure 3a). Since the dissolution and growth stages in model 1 could overlap temporally, correlating NU-1200 decay and STA-26 growth rates from time-resolved in situ PXRD does not provide enough information to distinguish the two models. Instead, we differentiate the conversion models using further experimental observations combined with energetic information.

One major distinction between the two models is the factor of new particle nucleation. If complete dissolution occurs (model 1), the original NU-1200 particles disappear, and new particles nucleate; if partial dissolution occurs (model 2), the original NU-1200 particle framework remains largely intact. To differentiate the two conversion models, we grew large $\sim\!100$ μm Zr-NU-1200 single crystals (Figure 3c) and exposed them to interpenetration conditions. If phase transformation follows model 1, we expect the NU-1200 crystals to transform into a STA-26 powder. Conversely, if phase transformation follows model 2, then we expect the NU-1200 crystals to transform into STA-26 crystals of the same morphology and size. After the conversion completed, we observed retained crystal size

(\sim 100 μ m) and morphology, supporting the partial dissolution model (Figure 3d). Bulk PXRD measurements of the same crystal batch before and after exposure to interpenetration conditions confirm that the phase transformation did, in fact, occur (Figure 3b).

Complementary SEM images tracking particle size and morphology during conversion also support the partial dissolution model (Figure S23). While the Zr-NU-1200 particles initiate their interpenetration journey as pristine, cubic crystals (Figure S23a), they first become damaged by etching (Figure S23b-c) but maintain their cubic morphology until conversion completion (S23d-e). This data strengthens the case for partial dissolution since the particle size distribution is maintained and pristine new nucleated particles are not observed.

Finally, we returned to the Avrami-Erofe'ev kinetic model (eq 1) to gather information about the sequential method of NU-1200 to STA-26 conversion. As mentioned above, the Avrami exponent, n, provides information about the mechanistic nature of crystallization. Values between 0.54 and 0.62 suggest a zero-order, diffusion-controlled mechanism; a firstorder, phase-boundary-controlled mechanism is indicated by values of 1.00-1.24; values between 2.00-3.00 designate a mechanism controlled by nucleation and growth. 38,50 Thus, in our system of interest, zero-order n values support model 1, while first-order n values strengthen model 2. We extracted Avrami exponents from sigmoidal crystallization curves of STA-26 growth at different temperatures (Figure 3e), particle sizes (Figure 3f), and formic acid concentrations (Figure 3g). In all cases, *n* values follow a first-order mechanism and remain similar for both the Zr and Hf systems. This data not only suggests that phase-boundary growth dominates but also indicates that the transformation mechanism is not affected by metal identity, temperature, particle size, or acid conditions (Figures S109-S111, Table S6). Taken together, these findings support our proposed model 2 of partial dissolution.

In conclusion, we report the first complete energy map of MOF interpenetration on a reaction energy landscape. Specifically, we monitor the phase transformation of NU-1200 to its doubly interpenetrated counterpart, STA-26 by pairing thermodynamic and kinetic data. Our DFT calculations show that the STA-26 frameworks are 3.69 kcal mol⁻¹ more stable than their NU-1200 counterparts with a similar density of states and electronic properties. While Zr-NU-1200 and Hf-NU-1200 interpenetrated to their STA-26 counterparts (likely driven by the increase in crystal density), Th-NU-1200 remained noninterpenetrated likely due to sterics. We implement Avrami-Erofe'ev modeling of time-resolved in situ X-ray diffraction to quantify rate constants and activation energies for the Zr- and Hf-NU-1200 transformations to Zrand Hf-STA-26, respectively. Observed differences in the activation energies of this transformation of Zr and Hf systems (25.2 and 27.9 kcal mol⁻¹, respectively), consistent with their metal-oxygen bond energies ($\Delta Hf_{Zr-O} = 182 \text{ kcal mol}^{-1}$, $\Delta Hf_{Hf-O} = 189 \text{ kcal mol}^{-1}$), reveal slower phase change kinetics for MOFs with stronger bonds. Additionally, this kinetic analysis is sensitive enough to experimentally reveal energetic differences between the two systems with similar metal-oxygen bond dissociation energies. Finally, we paired kinetic data with experimental observations to classify the mechanistic model of this phase transformation as partial dissolution. This study provides insight into MOF interpenetration, and the methodology used in this study can easily

be applied to other crystalline systems with parallel energetic similarities. More generally, we anticipate that this kinetic and mechanistic understanding will broadly inform further studies of the energetics of crystallization.

ASSOCIATED CONTENT

Data Availability Statement

The python code used for PXRD pattern background subtraction and peak integration is available at https://github.com/mbar11/insitupxrdareaunderthecurve.

Supporting Information

The Supporting Information is available free of charge at https://pubs.acs.org/doi/10.1021/acsmaterialslett.3c00598.

CIF files (ZIP) imol files (ZIP)

Materials, instrumentation, syntheses, NU-1200 characterization, ex-situ phase transformation of NU-1200 to STA-26, in-situ conversion of NU-1200 to STA-26, density functional theory (DFT) calculations, and supplementary schemes, figures, and tables (PDF)

AUTHOR INFORMATION

Corresponding Author

Omar K. Farha — Department of Chemistry and International Institute for Nanotechnology and Department of Chemical and Biological Engineering, Northwestern University, Evanston, Illinois 60208, United States; orcid.org/0000-0002-9904-9845; Email: o-farha@northwestern.edu

Authors

- Sylvia L. Hanna Department of Chemistry and International Institute for Nanotechnology, Northwestern University, Evanston, Illinois 60208, United States; orcid.org/0000-0003-3153-2416
- Michael Barsoum Department of Materials Science and Engineering, Northwestern University, Evanston, Illinois 60208, United States
- Tekalign Terfa Debela Department of Chemistry and Biochemistry, University of Oregon, Eugene, Oregon 97403, United States; © orcid.org/0000-0003-4859-2597
- Christos D. Malliakas Department of Chemistry and International Institute for Nanotechnology, Northwestern University, Evanston, Illinois 60208, United States; orcid.org/0000-0003-4416-638X
- Madeleine A. Gaidimas Department of Chemistry and International Institute for Nanotechnology, Northwestern University, Evanston, Illinois 60208, United States;
 occid.org/0000-0001-6111-8238
- Julia G. Knapp Department of Chemistry and International Institute for Nanotechnology, Northwestern University, Evanston, Illinois 60208, United States; ⊚ orcid.org/0000-0002-3324-4875
- Kent O. Kirlikovali Department of Chemistry and International Institute for Nanotechnology, Northwestern University, Evanston, Illinois 60208, United States;

 orcid.org/0000-0001-8329-1015
- Christopher H. Hendon Department of Chemistry and Biochemistry and Materials Science Institute, University of Oregon, Eugene, Oregon 97403, United States; orcid.org/0000-0002-7132-768X
- Vinayak P. Dravid Department of Materials Science and Engineering, International Institute for Nanotechnology, and

Northwestern University Atomic and Nanoscale Characterization Experimental Center, Northwestern University, Evanston, Illinois 60208, United States; orcid.org/0000-0002-6007-3063

Complete contact information is available at: https://pubs.acs.org/10.1021/acsmaterialslett.3c00598

Author Contributions

M.B. and T.T.D. contributed equally.

Author Contributions

O.K.F. supervised the project. S.L.H. and O.K.F. conceived the project and led the investigation, with the help of J.G.K.. S.L.H. designed the experiments, performed linker and MOF synthesis and characterization, prepared samples for and collected time-resolved *in situ* PXRD data, analyzed and fit the data to kinetic models, and interpreted the results. M.B. developed and ran the python script for analysis of *in situ* diffraction data under the supervision of V.P.D. and O.K.F.. T.T.D. performed DFT calculations under the supervision of C.H.H.. C.D.M. helped S.L.H. design time-resolved *in situ* PXRD experiments, adapted the STADI MP instrument for the desired collection design, and assisted S.L.H. with tuning of collection parameters. M.A.G. collected SEM images. S.L.H. and O.K.F. wrote the manuscript with the help of K.O.K., and all authors commented on and revised the manuscript.

Notes

The authors declare the following competing financial interest(s): Omar K. Farha has a financial interest in NuMat Technologies, a startup company that is seeking to commercialize MOFs. All other authors declare no competing interests. Large portions of this work were submitted to a pre-print server as part of S.L.H.'s Ph.D. thesis and can be found at the following citation in Chapter 4: Hanna, Sylvia L. Identifying Energy-Structure—Property Relationships in Uranium Metal—Organic Frameworks Through Their Dynamic Crystalline Structural Transformations. 2023, 30249970. Northwestern University ProQuest Dissertations Publishing. https://www.proquest.com/open/12pq-origsite=gscholar&cbl=18750&diss=y (accessed 2023-07-30).

ACKNOWLEDGMENTS

O.K.F., S.L.H., and J.G.K acknowledge support from the U.S. Department of Energy, National Nuclear Security Administration, under award number DE-NA0003763 and the U.S. Department of Energy award number DE-SC0022332. S.L.H. gratefully acknowledges support from the U.S. Department of Energy National Nuclear Security Administration Stewardship Science Graduate Fellowship (DOE NNSA SSGF) under award number DE-NA0003960. M.B. and V.P.D. acknowledge support from the Ryan Fellowship and the Department of Energy (DOE-BES DE-SC0022332). C.D.M. gratefully acknowledges support from Northwestern University. T.T.D. and C.H.H. are supported by the National Science Foundation under Grant No. [2237345] and the Camille and Henry Dreyfus Foundation. They are also grateful for access to the Extreme Science and Engineering Discovery Environment (XSEDE), which is supported by the National Science Foundation (ACI-1548562) and the PICS Coeus High Performance Computer, which is supported by the National Science Foundation (1624776). M.A.G. is supported by the Army Research Office under award number W911NF2020136.

J.G.K. is supported by the National Science Foundation (NSF) Graduate Research Fellowship under Grant No. DGE-2234667. K.O.K. gratefully acknowledges support from the IIN Postdoctoral Fellowship and the Northwestern University International Institute for Nanotechnology. This work made use of the Integrated Molecular Structure Education and Research Center (IMSERC) at Northwestern University, which has received support from the State of Illinois, Northwestern University, the Soft and Hybrid Nanotechnology Experimental (SHyNE) Resource (NSF ECCS-2025633), NSF CHE-1048773, and the International Institute for Nanotechnology (IIN). This work also made use of the Electron Probe Instrumentation Center (EPIC) of the Northwestern University Atomic and Nanoscale Characterization Experimental Center (NUANCE), which has received support from the SHyNE Resource (NSF ECCS-2025633), the IIN, and Northwestern's MRSEC program (NSF DMR-1720139). S.L.H. acknowledges Shengyi Su for his assistance in the early stages of this project, Prof. Austin M. Evans and Prof. Timur Islamoglu for thought-provoking conversations over the course of this project, and Nathaniel Barker for assistance with adjusting the STADI MP instrument hardware.

REFERENCES

- (1) Wang, Y.; He, J.; Liu, C.; Chong, W. H.; Chen, H. Thermodynamics versus Kinetics in Nanosynthesis. *Angew. Chem., Int. Ed.* **2015**, 54, 2022–2051.
- (2) Balluffi, R. W.; Allen, S. M.; Carter, W. C. Introduction. In *Kinetics of Materials*, 2005; pp 1–19.
- (3) Laidler, K. J. The development of the Arrhenius equation. J. Chem. Educ. 1984, 61, 494.
- (4) Cheetham, A. K.; Kieslich, G.; Yeung, H. H. M. Thermodynamic and Kinetic Effects in the Crystallization of Metal—Organic Frameworks. *Acc. Chem. Res.* **2018**, *51*, 659–667.
- (5) Bianchini, M.; Wang, J.; Clément, R. J.; Ouyang, B.; Xiao, P.; Kitchaev, D.; Shi, T.; Zhang, Y.; Wang, Y.; Kim, H.; Zhang, M.; Bai, J.; Wang, F.; Sun, W.; Ceder, G. The interplay between thermodynamics and kinetics in the solid-state synthesis of layered oxides. *Nat. Mater.* **2020**, *19*, 1088–1095.
- (6) Jana, G.; Pan, S.; Merino, G.; Chattaraj, P. K. MNgCCH (M = Cu, Ag, Au; Ng = Xe, Rn): The First Set of Compounds with M-Ng-C Bonding Motif. J. Phys. Chem. A 2017, 121, 6491-6499.
- (7) Tamayo, A. B.; Alleyne, B. D.; Djurovich, P. I.; Lamansky, S.; Tsyba, I.; Ho, N. N.; Bau, R.; Thompson, M. E. Synthesis and Characterization of Facial and Meridional Tris-cyclometalated Iridium(III) Complexes. J. Am. Chem. Soc. 2003, 125, 7377–7387.
- (8) Qin, Z.; Zhang, J.; Wan, C.; Liu, S.; Abroshan, H.; Jin, R.; Li, G. Atomically precise nanoclusters with reversible isomeric transformation for rotary nanomotors. *Nat. Commun.* **2020**, *11*, 6019.
- (9) Hua, X.; Liu, Z.; Fischer, M. G.; Borkiewicz, O.; Chupas, P. J.; Chapman, K. W.; Steiner, U.; Bruce, P. G.; Grey, C. P. Lithiation Thermodynamics and Kinetics of the TiO2 (B) Nanoparticles. *J. Am. Chem. Soc.* **2017**, *139*, 13330–13341.
- (10) Hatcher, L. E.; Skelton, J. M.; Warren, M. R.; Raithby, P. R. Photocrystallographic Studies on Transition Metal Nitrito Metastable Linkage Isomers: Manipulating the Metastable State. *Acc. Chem. Res.* **2019**, *52*, 1079–1088.
- (11) Lynch, M. S.; Cheng, M.; Van Kuiken, B. E.; Khalil, M. Probing the Photoinduced Metal—Nitrosyl Linkage Isomerism of Sodium Nitroprusside in Solution Using Transient Infrared Spectroscopy. *J. Am. Chem. Soc.* **2011**, *133*, 5255–5262.
- (12) Kirschner, M. S.; Diroll, B. T.; Guo, P.; Harvey, S. M.; Helweh, W.; Flanders, N. C.; Brumberg, A.; Watkins, N. E.; Leonard, A. A.; Evans, A. M.; Wasielewski, M. R.; Dichtel, W. R.; Zhang, X.; Chen, L. X.; Schaller, R. D. Photoinduced, reversible phase transitions in all-inorganic perovskite nanocrystals. *Nat. Commun.* **2019**, *10*, 504.

- (13) Bechtel, J. S.; Thomas, J. C.; Van der Ven, A. Finite-temperature simulation of anharmonicity and octahedral tilting transitions in halide perovskites. *Phys. Rev. Mater.* **2019**, *3*, 113605.
- (14) Jiang, Y.-s.; Yu, F.-d.; Que, L.-f.; Deng, L.; Xia, Y.; Ke, W.; Han, Y.; Wang, Z.-b. Revealing the Thermodynamics and Kinetics of In-Plane Disordered Li2MnO3 Structure in Li-Rich Cathodes. *ACS Energy Lett.* **2021**, *6*, 3836–3843.
- (15) Evans, J. D.; Bon, V.; Senkovska, I.; Lee, H.-C.; Kaskel, S. Four-dimensional metal-organic frameworks. *Nat. Commun.* **2020**, *11*, 2690–2700.
- (16) Kalmutzki, M. J.; Hanikel, N.; Yaghi, O. M. Secondary building units as the turning point in the development of the reticular chemistry of MOFs. *Sci. Adv.* **2018**, *4*, eaat9180.
- (17) Gong, Y.; Zhang, Y.; Qin, C.; Sun, C.; Wang, X.; Su, Z. Bottom-Up Construction and Reversible Structural Transformation of Supramolecular Isomers based on Large Truncated Tetrahedra. *Angew. Chem., Int. Ed.* **2019**, *58*, 780–784.
- (18) Ma, C.; Zheng, L.; Wang, G.; Guo, J.; Li, L.; He, Q.; Chen, Y.; Zhang, H. Phase engineering of metal-organic frameworks. *Aggregate* **2022**, *3*, e145.
- (19) Fan, W.-W.; Cheng, Y.; Zheng, L.-Y.; Cao, Q.-E. Reversible Phase Transition of Porous Coordination Polymers. *Chem.—Eur. J.* **2020**, *26*, 2766–2779.
- (20) Henkelis, S. E.; Vornholt, S. M.; Cordes, D. B.; Slawin, A. M. Z.; Wheatley, P. S.; Morris, R. E. A single crystal study of CPO-27 and UTSA-74 for nitric oxide storage and release. *CrystEngComm* **2019**, 21, 1857–1861.
- (21) Halder, A.; Ghoshal, D. Structure and properties of dynamic metal—organic frameworks: a brief accounts of crystalline-to-crystalline and crystalline-to-amorphous transformations. *CrystEng-Comm* **2018**, *20*, 1322—1345.
- (22) Gonzalez-Nelson, A.; Coudert, F.-X.; van der Veen, M. A. Rotational Dynamics of Linkers in Metal-Organic Frameworks. *Nanomaterials* **2019**, *9*, 330.
- (23) Zhao, P.; Tsang, S. C. E.; Fairen-Jimenez, D. Structural heterogeneity and dynamics in flexible metal-organic frameworks. *Cell Rep. Phys. Sci.* **2021**, *2*, 100544.
- (24) Redfern, L. R.; Farha, O. K. Mechanical properties of metalorganic frameworks. *Chem. Sci.* **2019**, *10*, 10666–10679.
- (25) Lapidus, S. H.; Halder, G. J.; Chupas, P. J.; Chapman, K. W. Exploiting high pressures to generate porosity, polymorphism, and lattice expansion in the nonporous molecular framework Zn(CN)2. *J. Am. Chem. Soc.* **2013**, *135*, 7621–7628.
- (26) Taylor, M. K.; Runčevski, T.; Oktawiec, J.; Gonzalez, M. I.; Siegelman, R. L.; Mason, J. A.; Ye, J.; Brown, C. M.; Long, J. R. Tuning the Adsorption-Induced Phase Change in the Flexible Metal—Organic Framework Co(bdp). *J. Am. Chem. Soc.* **2016**, *138*, 15019—15026
- (27) Wu, H.; Zhou, W.; Yildirim, T. Methane Sorption in Nanoporous Metal—Organic Frameworks and First-Order Phase Transition of Confined Methane. *J. Phys. Chem. C* **2009**, *113*, 3029—3035.
- (28) Zhang, J.; Kosaka, W.; Kitagawa, Y.; Miyasaka, H. A metalorganic framework that exhibits CO2-induced transitions between paramagnetism and ferrimagnetism. *Nat. Chem.* **2021**, *13*, 191–199.
- (29) Ferguson, A.; Liu, L.; Tapperwijn, S. J.; Perl, D.; Coudert, F.-X.; Van Cleuvenbergen, S.; Verbiest, T.; van der Veen, M. A.; Telfer, S. G. Controlled partial interpenetration in metal—organic frameworks. *Nat. Chem.* **2016**, *8*, 250–257.
- (30) Choi, S. B.; Furukawa, H.; Nam, H. J.; Jung, D.-Y.; Jhon, Y. H.; Walton, A.; Book, D.; O'Keeffe, M.; Yaghi, O. M.; Kim, J. Reversible Interpenetration in a Metal—Organic Framework Triggered by Ligand Removal and Addition. *Angew. Chem., Int. Ed.* **2012**, *51*, 8791–8795.
- (31) Jiang, H.-L.; Makal, T. A.; Zhou, H.-C. Interpenetration control in metal—organic frameworks for functional applications. *Coord. Chem. Rev.* **2013**, 257, 2232–2249.
- (32) Novendra, N.; Marrett, J. M.; Katsenis, A. D.; Titi, H. M.; Arhangelskis, M.; Friščić, T.; Navrotsky, A. Linker Substituents

- Control the Thermodynamic Stability in Metal—Organic Frameworks. *J. Am. Chem. Soc.* **2020**, 142, 21720—21729.
- (33) Sun, H.; Wu, D. Recent advances in experimental thermodynamics of metal-organic frameworks. *Powder Diffr.* **2019**, 34, 297–301.
- (34) Bara, D. J.; Wilson, C.; Mörtel, M.; Khusniyarov, M. M.; Ling, S.; Slater, B.; Sproules, S.; Forgan, R. S. Kinetic control of interpenetration in Fe-biphenyl-4,4'-dicarboxylate metal-organic frameworks by coordination and oxidation modulation. *J. Am. Chem. Soc.* **2019**, *141*, 8346–8357.
- (35) Lyu, J.; Gong, X.; Lee, S.-J.; Gnanasekaran, K.; Zhang, X.; Wasson, M. C.; Wang, X.; Bai, P.; Guo, X.; Gianneschi, N. C.; Farha, O. K. Phase Transitions in Metal—Organic Frameworks Directly Monitored through In Situ Variable Temperature Liquid-Cell Transmission Electron Microscopy and In Situ X-ray Diffraction. *J. Am. Chem. Soc.* 2020, 142, 4609—4615.
- (36) Widmer, R. N.; Lampronti, G. I.; Chibani, S.; Wilson, C. W.; Anzellini, S.; Farsang, S.; Kleppe, A. K.; Casati, N. P. M.; MacLeod, S. G.; Redfern, S. A. T.; Coudert, F.-X.; Bennett, T. D. Rich Polymorphism of a Metal—Organic Framework in Pressure—Temperature Space. *J. Am. Chem. Soc.* **2019**, *141*, 9330—9337.
- (37) Friščić, T.; Halasz, I.; Beldon, P. J.; Belenguer, A. M.; Adams, F.; Kimber, S. A. J.; Honkimäki, V.; Dinnebier, R. E. Real-time and in situ monitoring of mechanochemical milling reactions. *Nat. Chem.* **2013**, *5*, 66–73.
- (38) Walton, R. I.; Millange, F. In Situ Studies of the Crystallization of Metal—Organic Frameworks. In *The Chemistry of Metal—Organic Frameworks: Synthesis, Characterization, and Applications*; 2016; pp 729—764.
- (39) Feyand, M.; Hübner, A.; Rothkirch, A.; Wragg, D. S.; Stock, N. Copper Phosphonatoethanesulfonates: Temperature Dependent in Situ Energy Dispersive X-ray Diffraction Study and Influence of the pH on the Crystal Structures. *Inorg. Chem.* **2012**, *51*, 12540–12547. (40) Ragon, F.; Horcajada, P.; Chevreau, H.; Hwang, Y. K.; Lee, U. H.; Miller, S. R.; Devic, T.; Chang, J.-S.; Serre, C. In Situ Energy-Dispersive X-ray Diffraction for the Synthesis Optimization and Scale-up of the Porous Zirconium Terephthalate UiO-66. *Inorg. Chem.* **2014**, *53*, 2491–2500.
- (41) Yeung, H. H. M.; Wu, Y.; Henke, S.; Cheetham, A. K.; O'Hare, D.; Walton, R. I. In Situ Observation of Successive Crystallizations and Metastable Intermediates in the Formation of Metal—Organic Frameworks. *Angew. Chem., Int. Ed.* **2016**, *55*, 2012–2016.
- (42) Bumstead, A. M.; Cordes, D. B.; Dawson, D. M.; Chakarova, K. K.; Mihaylov, M. Y.; Hobday, C. L.; Duren, T.; Hadjiivanov, K. I.; Slawin, A. M. Z.; Ashbrook, S. E.; Prasad, R. R. R.; Wright, P. A. Modulator-Controlled Synthesis of Microporous STA-26, an Interpenetrated 8,3-Connected Zirconium MOF with the the-i Topology, and its Reversible Lattice Shift. *Chem.—Eur. J.* 2018, 24, 6115–6126.
- (43) Liu, T. F.; Vermeulen, N. A.; Howarth, A. J.; Li, P.; Sarjeant, A. A.; Hupp, J. T.; Farha, O. K. Adding to the Arsenal of Zirconium-Based Metal-Organic Frameworks: the Topology as a Platform for Solvent-Assisted Metal Incorporation. *Eur. J. Inorg. Chem.* **2016**, 2016, 4349–4352.
- (44) Wang, B.; Lv, X. L.; Feng, D.; Xie, L. H.; Zhang, J.; Li, M.; Xie, Y.; Li, J. R.; Zhou, H. C. Highly Stable Zr(IV)-Based Metal-Organic Frameworks for the Detection and Removal of Antibiotics and Organic Explosives in Water. J. Am. Chem. Soc. 2016, 138, 6204–16. (45) Wang, X.; Zhang, X.; Li, P.; Otake, K.-i.; Cui, Y.; Lyu, J.; Krzyaniak, M. D.; Zhang, Y.; Li, Z.; Liu, J.; Buru, C. T.; Islamoglu, T.; Wasielewski, M. R.; Li, Z.; Farha, O. K. Vanadium Catalyst on Isostructural Transition Metal, Lanthanide, and Actinide Based Metal–Organic Frameworks for Alcohol Oxidation. J. Am. Chem. Soc. 2019, 141, 8306–8314.
- (46) Robison, L.; Gong, X.; Evans, A. M.; Son, F. A.; Wang, X.; Redfern, L. R.; Wasson, M. C.; Syed, Z. H.; Chen, Z.; Idrees, K. B.; Islamoglu, T.; Delferro, M.; Dichtel, W. R.; Coudert, F.-X.; Gianneschi, N. C.; Farha, O. K. Transient Catenation in a Zirconium-Based Metal—Organic Framework and Its Effect on

- Mechanical Stability and Sorption Properties. J. Am. Chem. Soc. 2021, 143, 1503–1512.
- (47) Wu, Y.; Henke, S.; Kieslich, G.; Schwedler, I.; Yang, M.; Fraser, D. A. X.; O'Hare, D. Time-Resolved In Situ X-ray Diffraction Reveals Metal-Dependent Metal—Organic Framework Formation. *Angew. Chem., Int. Ed.* **2016**, *55*, 14081—14084.
- (48) Forgan, R. S. Modulated self-assembly of metal-organic frameworks. *Chem. Sci.* **2020**, *11*, 4546–4562.
- (49) Kirlikovali, K. O.; Chen, Z.; Wang, X.; Mian, M. R.; Alayoglu, S.; Islamoglu, T.; Farha, O. K. Investigating the Influence of Hexanuclear Clusters in Isostructural Metal—Organic Frameworks on Toxic Gas Adsorption. ACS Appl. Mater. Interfaces 2022, 14, 3048—3056.
- (50) Jensen, K. M. Ø.; Tyrsted, C.; Bremholm, M.; Iversen, B. B. In Situ Studies of Solvothermal Synthesis of Energy Materials. *ChemSusChem* **2014**, *7*, 1594–1611.
- (51) Van Vleet, M. J.; Weng, T.; Li, X.; Schmidt, J. R. In Situ, Time-Resolved, and Mechanistic Studies of Metal-Organic Framework Nucleation and Growth. *Chem. Rev.* **2018**, *118*, 3681-3721.
- (52) Avrami, M. Kinetics of Phase Change. I General Theory. J. Chem. Phys. 1939, 7, 1103–1112.
- (53) Avrami, M. Kinetics of Phase Change. II Transformation-Time Relations for Random Distribution of Nuclei. *J. Chem. Phys.* **1940**, *8*, 212–224.
- (54) Avrami, M. Granulation, Phase Change, and Microstructure Kinetics of Phase Change. III. *J. Chem. Phys.* **1941**, *9*, 177–184.
- (55) Henkelis, S. E.; Mazur, M.; Rice, C. M.; Wheatley, P. S.; Ashbrook, S. E.; Morris, R. E. Kinetics and Mechanism of the Hydrolysis and Rearrangement Processes within the Assembly—Disassembly—Organization—Reassembly Synthesis of Zeolites. *J. Am. Chem. Soc.* **2019**, *141*, 4453—4459.
- (56) Walton, R. I.; Millange, F.; O'Hare, D.; Davies, A. T.; Sankar, G.; Catlow, C. R. A. An in Situ Energy-Dispersive X-ray Diffraction Study of the Hydrothermal Crystallization of Zeolite A. 1. Influence of Reaction Conditions and Transformation into Sodalite. *J. Phys. Chem. B* **2001**, *105*, 83–90.
- (57) Kadja, G. T. M.; Azhari, N. J.; Mukti, R. R.; Khalil, M. A Mechanistic Investigation of Sustainable Solvent-Free, Seed-Directed Synthesis of ZSM-5 Zeolites in the Absence of an Organic Structure-Directing Agent. ACS Omega 2021, 6, 925–933.
- (58) Martell, J. D.; Milner, P. J.; Siegelman, R. L.; Long, J. R. Kinetics of cooperative CO2 adsorption in diamine-appended variants of the metal—organic framework Mg2(dobpdc). *Chem. Sci.* **2020**, *11*, 6457–6471.
- (59) Widmer, R. N.; Lampronti, G. I.; Casati, N.; Farsang, S.; Bennett, T. D.; Redfern, S. A. T. X-ray radiation-induced amorphization of metal—organic frameworks. *Phys. Chem. Chem. Phys.* **2019**, 21, 12389—12395.
- (60) Das, C.; Nishiguchi, T.; Fan, Z.; Horike, S. Crystallization Kinetics of a Liquid-Forming 2D Coordination Polymer. *Nano Lett.* **2022**, 22, 9372–9379.
- (61) Donakowski, A.; Miller, D. W.; Anderson, N. C.; Ruth, A.; Sanehira, E. M.; Berry, J. J.; Irwin, M. D.; Rockett, A.; Steirer, K. X. Improving Photostability of Cesium-Doped Formamidinium Lead Triiodide Perovskite. ACS Energy Lett. 2021, 6, 574–580.
- (62) Ok, K. M.; Lee, D. W.; Smith, R. I.; O'Hare, D. Time-Resolved in Situ Neutron Diffraction under Supercritical Hydrothermal Conditions: A Study of the Synthesis of KTiOPO4. *J. Am. Chem. Soc.* **2012**, *134*, 17889–17891.